

# Triazolone-Functionalized Magnetic Nanoparticles for Hemoglobin Purification and Proteomics-Driven Biomarker Discovery in Diabetic Blood

Xinze Wu,<sup>#</sup> Lingxi Zhang,<sup>#</sup> Tian Luan, Ying Wang, Xiangyu Liu, Mingsheng Zhou,<sup>\*</sup> Fu Ren,<sup>\*</sup> Qing Chen,<sup>\*</sup> Xifan Mei, Xuwei Chen, and Jianhua Wang



Cite This: *Anal. Chem.* 2025, 97, 10396–10404



Read Online

ACCESS |



Metrics & More

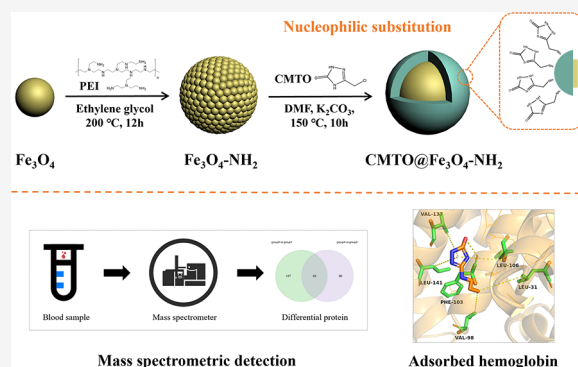


Article Recommendations



Supporting Information

**ABSTRACT:** Hemoglobin, particularly glycated hemoglobin, serves as the gold standard for diagnosing diabetes in clinical settings. In this study, a triazolone derivative, 3-chloromethyl-1,2,4-triazol-5-one (CMTO), was conjugated to polyethylenimine-modified magnetic nanoparticles via an amination reaction, resulting in the formation of a novel composite material, CMTO@Fe<sub>3</sub>O<sub>4</sub>-NH<sub>2</sub>. Molecular simulations revealed that the carbonyl group of CMTO underwent tautomerization to an enol form under neutral pH conditions. The enol form established hydrogen bonds with phenylalanine residues in hemoglobin, while the triazole ring interacted with the hemoglobin  $\beta$ -subunit through  $\pi$ - $\pi$  interactions. These interactions significantly enhanced the performance of CMTO@Fe<sub>3</sub>O<sub>4</sub>-NH<sub>2</sub> in the effective separation and purification of hemoglobin. Specifically, 1.0 mg of CMTO@Fe<sub>3</sub>O<sub>4</sub>-NH<sub>2</sub> successfully adsorbed hemoglobin from 0.5 mL of a 100  $\mu$ g mL<sup>-1</sup> hemoglobin solution, with an excellent adsorption efficiency of 93.8% in just 45 min. The adsorption process was found to follow the Langmuir model with a theoretical adsorption capacity of 344.83 mg g<sup>-1</sup>. Furthermore, with a 91.2% elution efficiency, the adsorbed hemoglobin could be efficiently eluted using a 100 mmol L<sup>-1</sup> imidazole solution. After five cycles, the material retained 88.1% of its initial adsorption efficiency. Encouraged by its hemoglobin adsorption efficiency, the composite material was applied to selectively separate hemoglobin from human whole blood. Protein sequencing identified 1114 proteins in this process, with 252 differential proteins found between diabetic and healthy individuals. Pathway analysis and protein-protein interaction (PPI) networks identified 12 potential diabetic biomarkers.



## INTRODUCTION

Magnetic nanoparticle-based capture materials have emerged as a research focus in materials science, driven by their distinctive physicochemical characteristics and promising application potential in recent years. These nanoparticles possess a large specific surface area<sup>1</sup> and high adsorption capacity,<sup>2</sup> which facilitate the rapid adsorption of target molecules and fast separation using an external magnetic field. Moreover, the surface of the magnetic nanoparticles can be easily modified to introduce various functional groups,<sup>3</sup> enabling the selective capture of specific proteins or biomarkers.<sup>4–6</sup> Additionally, functionalized nanoparticle formulations have been reported to achieve higher therapeutic efficacy compared to traditional drugs.<sup>7,8</sup> This enhanced efficacy can be attributed to the functionalization of the nanoparticle surface, which can be coupled with organic molecules,<sup>3</sup> antibodies,<sup>9</sup> nucleic acids,<sup>10</sup> ligands,<sup>11</sup> and drugs,<sup>12</sup> thereby improving solubility, biocompatibility, and specific targeting ability.<sup>13,14</sup> Raquel Petrioli<sup>9</sup> demonstrated that conjugating monoclonal antibodies to nanoparticles enabled targeted therapy for various types of tumors.

Recent advancements in genomics, proteomics, and metabolomics<sup>15,16</sup> have elevated analytical techniques for biomarker discovery to new heights. Among these, liquid chromatography–mass spectrometry (LC-MS) stands out for its superior sensitivity, selectivity, and identification capability for proteomics.<sup>17–19</sup> LC-MS can also analyze the majority of protein components in blood. However, plasma proteomics analysis faces significant technical challenges due to the high dynamic range of plasma protein concentrations (more than 10<sup>10</sup>) and the complexity of the proteome.<sup>20</sup> These challenges make appropriate sample preprocessing a critical and necessary step. Effective sample preparation can remove interfering substances<sup>21</sup> and enrich biomarkers,<sup>22</sup> thereby improving the

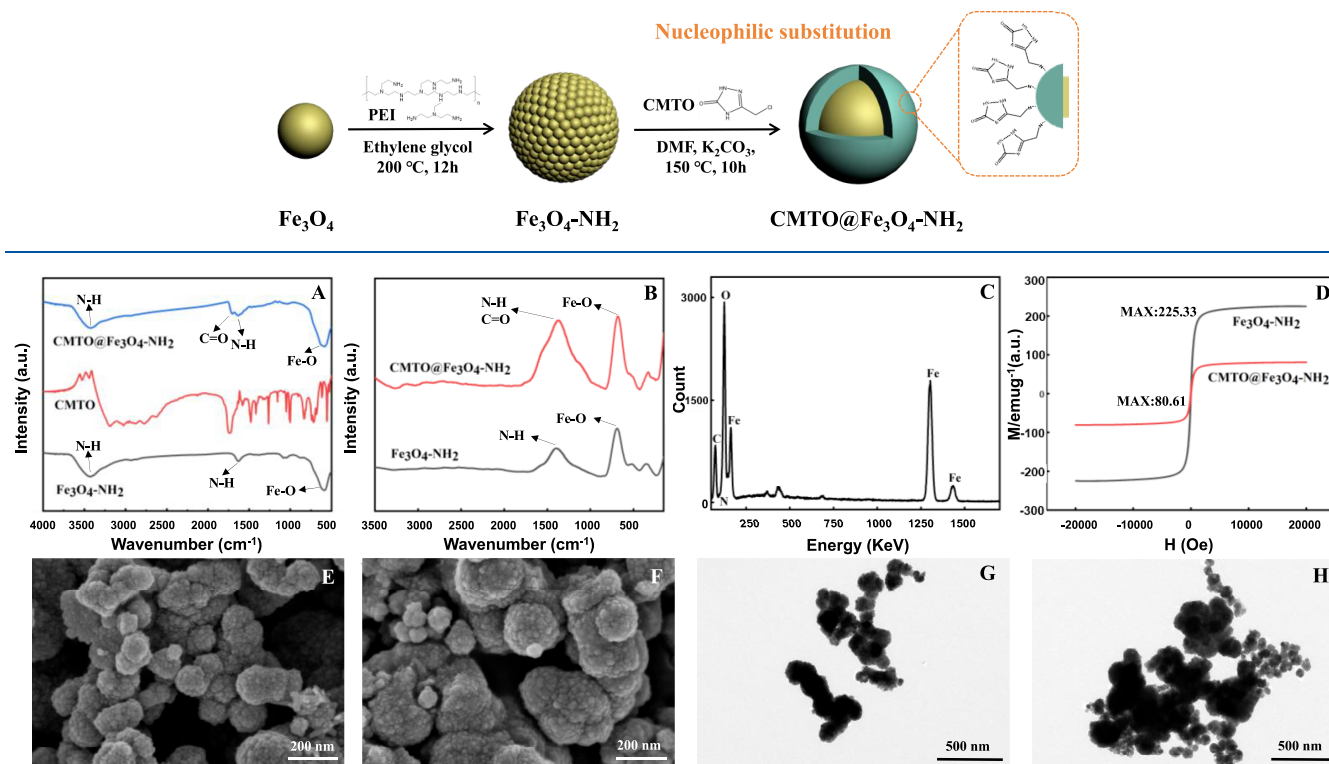
**Received:** February 4, 2025

**Revised:** May 5, 2025

**Accepted:** May 5, 2025

**Published:** May 9, 2025



Scheme 1. Schematic Representation of the Synthesis of CMTO@Fe<sub>3</sub>O<sub>4</sub>-NH<sub>2</sub> via Nucleophilic Substitution

**Figure 1.** FT-IR spectra of Fe<sub>3</sub>O<sub>4</sub>-NH<sub>2</sub>, CMTO and CMTO@Fe<sub>3</sub>O<sub>4</sub>-NH<sub>2</sub> (A); Raman spectra of Fe<sub>3</sub>O<sub>4</sub>-NH<sub>2</sub> and CMTO@Fe<sub>3</sub>O<sub>4</sub>-NH<sub>2</sub> (B); EDS analysis of CMTO@Fe<sub>3</sub>O<sub>4</sub>-NH<sub>2</sub> (C); VSM curves of Fe<sub>3</sub>O<sub>4</sub>-NH<sub>2</sub> and CMTO@Fe<sub>3</sub>O<sub>4</sub>-NH<sub>2</sub> (D); SEM images of Fe<sub>3</sub>O<sub>4</sub>-NH<sub>2</sub> and CMTO@Fe<sub>3</sub>O<sub>4</sub>-NH<sub>2</sub> (E, F) and TEM images of Fe<sub>3</sub>O<sub>4</sub>-NH<sub>2</sub> and CMTO@Fe<sub>3</sub>O<sub>4</sub>-NH<sub>2</sub> (G, H).

accuracy and precision of the detection. For instance, Monopoli et al. utilized Nanoparticle Biomolecular Corona to enrich glycoproteins for *N*-glycan profiling, which was applied in biomarker discovery. This approach successfully identified several glycoproteins and *N*-glycan peaks that exhibited significant differences between lung cancer patients and healthy controls.<sup>23</sup>

By conjugating the triazole-phosphine analog 3-chloromethyl-1,2,4-triazol-5-one (CMTO) to PEI-modified magnetic nanoparticles via an amination reaction, a novel composite material, CMTO@Fe<sub>3</sub>O<sub>4</sub>-NH<sub>2</sub>, was prepared in this study. The prepared composite demonstrated excellent adsorption selectivity for hemoglobin owing to the strong interaction between the triazole ring and the hemoglobin  $\beta$ -subunit. Encouraged by the above results, a novel method was established for isolating and purifying hemoglobin from human whole blood. The results revealed that CMTO@Fe<sub>3</sub>O<sub>4</sub>-NH<sub>2</sub> significantly enhanced hemoglobin separation, providing a reliable and efficient approach for processing blood samples. Additionally, protein sequencing of whole blood samples from both diabetic and healthy individuals was done to identify potential biomarkers for diabetes. Enrichment analysis, in conjunction with differential protein network interaction analysis, identified 12 potential diabetic biomarkers: *SAA1*, *SAA2*, *CRP*, *SERPINA3*, *ITIH3*, *PRDX4*, *EIF2S1*, *THBS1*, *APOL1*, *APOE*, *APOB*, and *CFP*. These biomarkers provide critical insights into the pathology of diabetes and represent promising targets for therapeutic intervention.

## EXPERIMENTAL SECTION

**Preparation of CMTO@Fe<sub>3</sub>O<sub>4</sub>-NH<sub>2</sub>.** Here, the solvent-thermal method was used to synthesize the amino-coated magnetic nanoparticles (Fe<sub>3</sub>O<sub>4</sub>-NH<sub>2</sub>), using polyethylenimine (PEI) acting as a protective agent.<sup>24</sup> First, 3-chloromethyl-1,2,4-triazoline-5-one (0.24 g) was dissolved in DMF (50 mL), followed by the addition of Fe<sub>3</sub>O<sub>4</sub>-NH<sub>2</sub> (10 mg) and potassium carbonate (0.345 g). The mixture was refluxed with condensation at 150 °C for 10 h and then cooled naturally to room temperature. The obtained product was washed thrice each with DMF and with water until a neutral pH was achieved. Finally, the product was dried at 60 °C for 12 h to obtain CMTO@Fe<sub>3</sub>O<sub>4</sub>-NH<sub>2</sub>.

**Isolation and Identification of Hemoglobin from Actual Samples by CMTO@Fe<sub>3</sub>O<sub>4</sub>-NH<sub>2</sub>.** Whole blood samples from 5 healthy individuals and 5 patients with diabetes were collected from a local hospital. The whole blood sample was frozen at -20 °C for 6 h, thawed at room temperature, shaken and mixed, repeated freeze-thaw 3 times, fully lysed red blood cells to release hemoglobin.<sup>25</sup> Then the samples from the healthy group and the diabetes group were mixed to obtain two combined whole blood samples. A Britton-Robinson (BR) solution (pH 7) was used to prepare a 1000-fold dilution of the whole blood samples. CMTO@Fe<sub>3</sub>O<sub>4</sub>-NH<sub>2</sub> (1.0 mg) was added to 500  $\mu$ L of the diluted whole blood sample and then shaken for 45 min. After removing the supernatant, 500  $\mu$ L of deionized water (ddH<sub>2</sub>O) was added to the mixture and shaken for 15 min, followed by magnetic separation to remove the supernatant. Finally, 100 mmol L<sup>-1</sup>

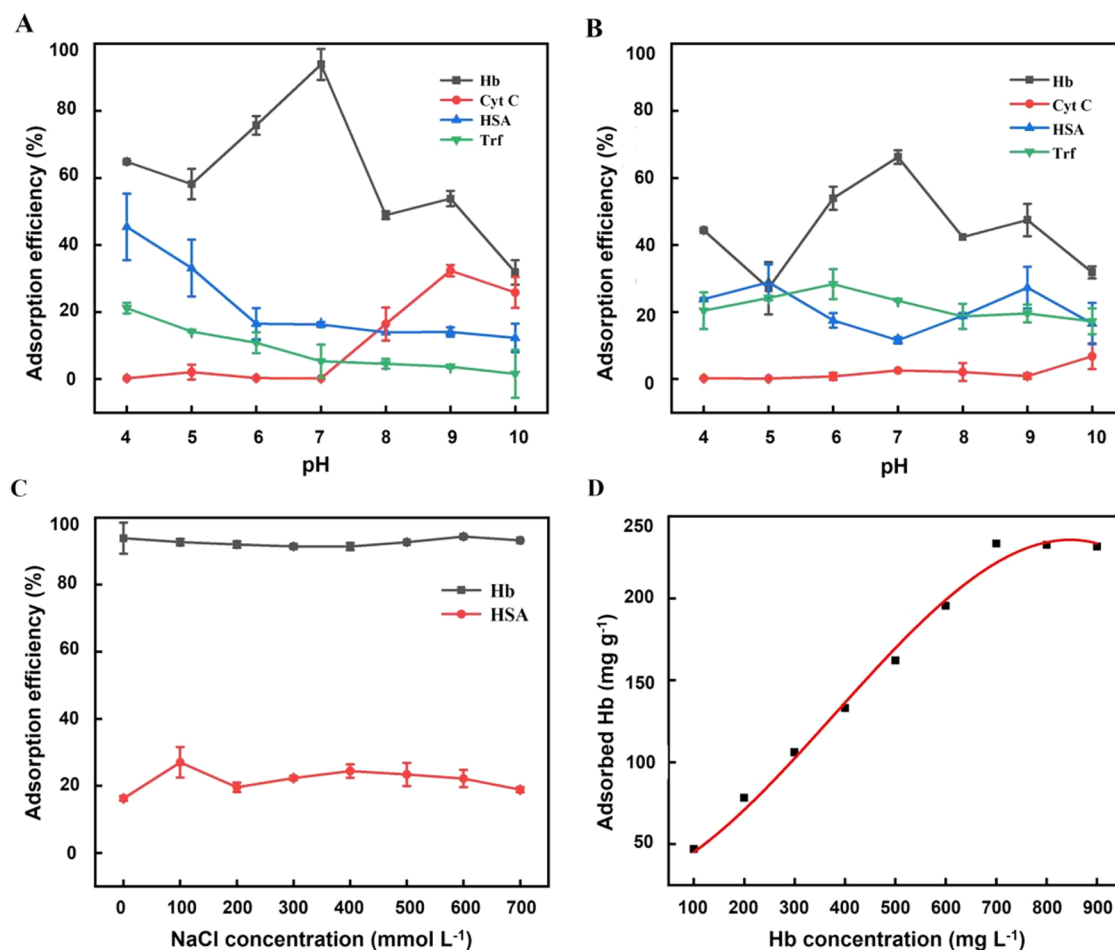


**Figure 2.** Effect of pH on adsorption efficiency of Hb, Cyt-C, HSA, and Trf onto CMTO@Fe<sub>3</sub>O<sub>4</sub>-NH<sub>2</sub> (A) and Fe<sub>3</sub>O<sub>4</sub>-NH<sub>2</sub> (B); Effect of ionic strength on the adsorption behaviors of Hb and HSA with CMTO@Fe<sub>3</sub>O<sub>4</sub>-NH<sub>2</sub> as adsorbent (C); Adsorption isotherm of Hb by the CMTO@Fe<sub>3</sub>O<sub>4</sub>-NH<sub>2</sub> composite (D).

imidazole solution (500  $\mu$ L) was added, and the mixture was eluted for 30 min, obtaining purified hemoglobin.

## RESULTS AND DISCUSSION

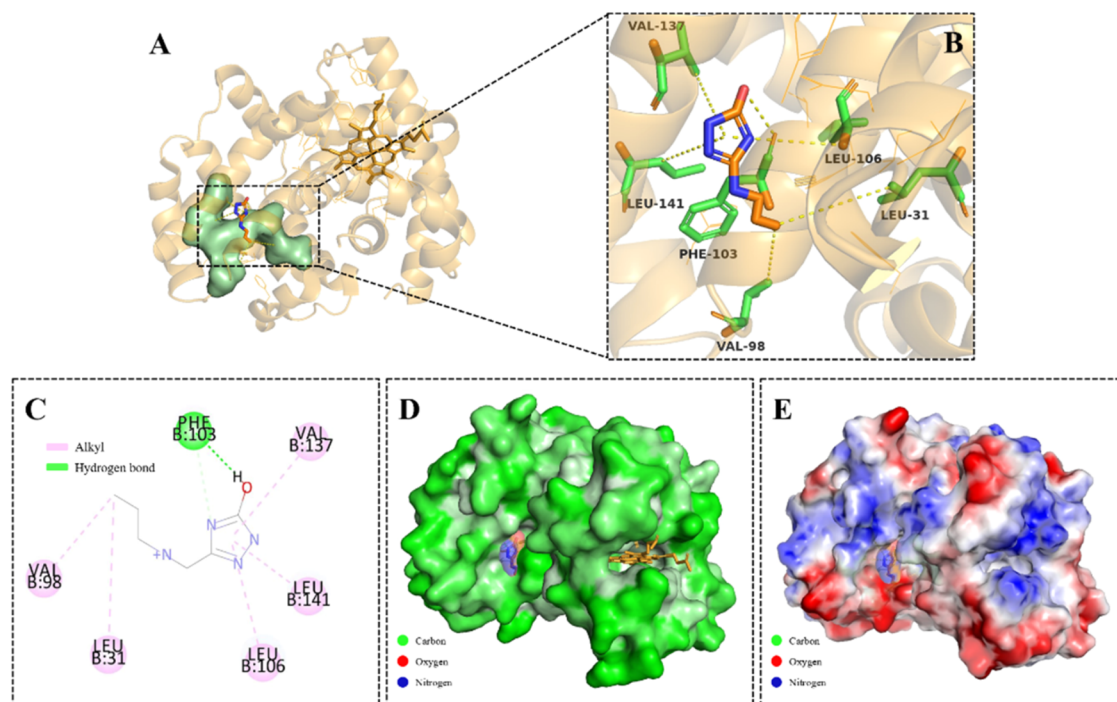
**Characterization of the CMTO@Fe<sub>3</sub>O<sub>4</sub>-NH<sub>2</sub>.** This study synthesized the composite material, Fe<sub>3</sub>O<sub>4</sub>-NH<sub>2</sub> nanoparticles, via the solvothermal method. Polyethylenimine (PEI) was employed as a stabilizing agent to prevent particle aggregation and introduce a high density of amino (-NH<sub>2</sub>) functional groups on the surface of the magnetic nanoparticles.<sup>26</sup> Through the selection and optimization of the reaction solvent with experiments, dimethylformamide (DMF) was selected as the reaction solvent because of its good solvation properties and ability to promote reaction conditions. The abundant amino groups on the surface of Fe<sub>3</sub>O<sub>4</sub>-NH<sub>2</sub> participated in a bimolecular nucleophilic substitution reaction with 3-chloromethyl-1,2,4-triazoline-5-one (CMTO), leading to the successful functionalization of the magnetic nanoparticles with a CMTO coating.<sup>27–29</sup> The role of K<sub>2</sub>CO<sub>3</sub> is to provide an alkaline environment to promote nucleophilic substitution, and the specific mechanism is to enhance the reactivity of CMTO through deprotonation. This functionalization improves the chemical reactivity and expands the application potential of Fe<sub>3</sub>O<sub>4</sub>-NH<sub>2</sub> nanoparticles by introducing additional reactive sites via the CMTO moieties (Scheme 1).

Figure 1A shows the Fourier-transform infrared (FT-IR) spectra of Fe<sub>3</sub>O<sub>4</sub>-NH<sub>2</sub> and CMTO@Fe<sub>3</sub>O<sub>4</sub>-NH<sub>2</sub>. The FT-IR spectrum of Fe<sub>3</sub>O<sub>4</sub>-NH<sub>2</sub> exhibited a distinct absorption peak at 586 cm<sup>-1</sup>, corresponding to the Fe-O bond vibrational mode, which is a characteristic feature of the magnetite lattice structure. Meanwhile, the absorption bands at 1631 cm<sup>-1</sup> and 3423 cm<sup>-1</sup> could be attributed to the N-H stretching vibrations in the -NH<sub>2</sub> functional groups (R-NH<sub>2</sub>). The presence of these peaks in the FT-IR spectrum of Fe<sub>3</sub>O<sub>4</sub>-NH<sub>2</sub> serves as strong evidence of a substantial concentration of amino groups on the surface of the magnetic nanoparticles. Following CMTO modification, the FT-IR spectrum of CMTO@Fe<sub>3</sub>O<sub>4</sub>-NH<sub>2</sub> revealed the presence of a strong absorption peak at 1703 cm<sup>-1</sup>, corresponding to a carbonyl (C=O) stretching vibration. This peak, which was absent in the spectrum of unmodified Fe<sub>3</sub>O<sub>4</sub>-NH<sub>2</sub>, confirmed the successful interaction of CMTO onto the nanoparticle surface, providing clear evidence of successful functionalization.

Figure 1B illustrates the Raman spectra of Fe<sub>3</sub>O<sub>4</sub>-NH<sub>2</sub> and CMTO@Fe<sub>3</sub>O<sub>4</sub>-NH<sub>2</sub>. The spectrum of Fe<sub>3</sub>O<sub>4</sub>-NH<sub>2</sub> revealed an absorption peak at 1380 cm<sup>-1</sup> attributed to the N-H bending vibration of the amino groups. Additionally, the peak at 689 cm<sup>-1</sup> corresponded to the Raman lattice stretching vibration of Fe<sub>3</sub>O<sub>4</sub>. Upon coating Fe<sub>3</sub>O<sub>4</sub>-NH<sub>2</sub> with CMTO, the intensity of the 1380 cm<sup>-1</sup> peak in the Raman spectrum of the resulting CMTO@Fe<sub>3</sub>O<sub>4</sub>-NH<sub>2</sub> was significantly increased.



**Scheme 2.** Molecular Docking Analysis of Hb with CMTO (A); Lowest Energy Conformation of the Docking of Hb and CMTO (B); Detailed 3D Image of the Binding Mode of the Hb and CMTO (C); Hydrophilic and Hydrophobic Interactions (D); Electrostatic Potential Energy Distribution of the Protein Surface (E)



compared to  $\text{Fe}_3\text{O}_4\text{-NH}_2$ . This enhancement could be attributed to the overlap of the carbonyl absorption band of the 3-chloromethyl-1,2,4-triazoline-5-one (at approximately  $1675\text{ cm}^{-1}$ ) with the amino N–H bending vibration, indicating the successful functionalization of  $\text{Fe}_3\text{O}_4\text{-NH}_2$  with CMTO. The functionalization likely altered the electronic structure and vibrational properties of the surface-bound amino groups.<sup>30</sup>

As shown in Figure 1C, the energy-dispersive X-ray spectroscopy (EDS) spectrum of  $\text{CMTO@Fe}_3\text{O}_4\text{-NH}_2$  confirmed the presence of Fe, C, O, and N elements. This elemental composition confirms the successful attachment of CMTO on the surface of the  $\text{Fe}_3\text{O}_4\text{-NH}_2$  magnetic nanoparticles. Figure 1D shows that the saturation magnetization of  $\text{Fe}_3\text{O}_4\text{-NH}_2$  was approximately  $225.33\text{ emu g}^{-1}$ , which decreased to  $80.61\text{ emu g}^{-1}$  after CMTO modification. This reduction was attributed to the nonmagnetic CMTO coating on the  $\text{Fe}_3\text{O}_4\text{-NH}_2$  surface. However, despite the decline,  $\text{CMTO@Fe}_3\text{O}_4\text{-NH}_2$  maintained strong superparamagnetic properties, making it suitable for magnetic separation applications.

The SEM images of  $\text{Fe}_3\text{O}_4\text{-NH}_2$  and  $\text{CMTO@Fe}_3\text{O}_4\text{-NH}_2$  are shown in Figure 1E,F, respectively, while their corresponding TEM images are shown in Figure 1G,H, respectively. As shown in Figure 1E,I,G, the synthesized  $\text{Fe}_3\text{O}_4\text{-NH}_2$  comprised numerous small particles that coalesce into larger spherical aggregates, approximately 150 nm in diameter. This aggregation could be attributed to the presence of high molecular-weight polymers, such as PEI, which facilitate the connection of multiple particles to form larger structures. In contrast, Figure 1F,H illustrate that CMTO-modified magnetic nanoparticles exhibited smoother surfaces and an increased size, approximately 250 nm. The CMTO coating encapsulated the  $\text{Fe}_3\text{O}_4\text{-NH}_2$  particles, masking their original

dimensions, resulting in larger and more uniform spherical particles.

#### Protein Adsorption Behaviors of $\text{CMTO@Fe}_3\text{O}_4\text{-NH}_2$ .

The protein adsorption behavior of  $\text{CMTO@Fe}_3\text{O}_4\text{-NH}_2$  was studied to evaluate its affinity for different proteins. Four model proteins were selected for this study: human serum albumin (HSA, pI 4.9), transferrin (Trf, pI 5.4), cytochrome C (Cyt-C, pI 9.8–10.1), and human hemoglobin (Hb, pI 6.8–7.0). Figure 2A presents the adsorption efficiency of  $\text{CMTO@Fe}_3\text{O}_4\text{-NH}_2$  for the selected proteins over a pH range of 4.0 to 10.0. With increasing pH, Hb exhibited an initial rise in adsorption efficiency, followed by a gradual decline. In contrast, the adsorption efficiency for HSA and Trf steadily decreased with an increase in pH. For Cyt-C, the adsorption efficiency of the composite steadily increased with an increase in pH. Notably, the adsorption efficiency of  $\text{CMTO@Fe}_3\text{O}_4\text{-NH}_2$  for Hb reached 93.8% at pH 7.0, whereas the adsorption efficiencies for HSA, Trf, and Cyt-C remained below 20.0%. These findings highlight that  $\text{CMTO@Fe}_3\text{O}_4\text{-NH}_2$  exhibited strong selectivity for Hb adsorption. Figure 2B presents the adsorption efficiency of  $\text{Fe}_3\text{O}_4\text{-NH}_2$ , the adsorption efficiency of  $\text{Fe}_3\text{O}_4\text{-NH}_2$  for Hb is limited to 66.2%.

Ionic strength plays a crucial role in modulating the interaction between protein molecules and solid-phase materials. As shown in Figure 2C, this study investigated the impact of NaCl concentrations on the adsorption efficiencies of Hb and HSA at pH 7.0. With an increase in NaCl concentration, the adsorption efficiency of  $\text{CMTO@Fe}_3\text{O}_4\text{-NH}_2$  remained stable above 90.0% for Hb. Moreover, salt compresses the protein's electrical double layer, reducing electrostatic repulsion between adsorbed proteins, thereby enhancing adsorption efficiency. As a result, Hb adsorption remains largely unaffected by high salt concentrations, demonstrating stable adsorption across varying ionic strengths.



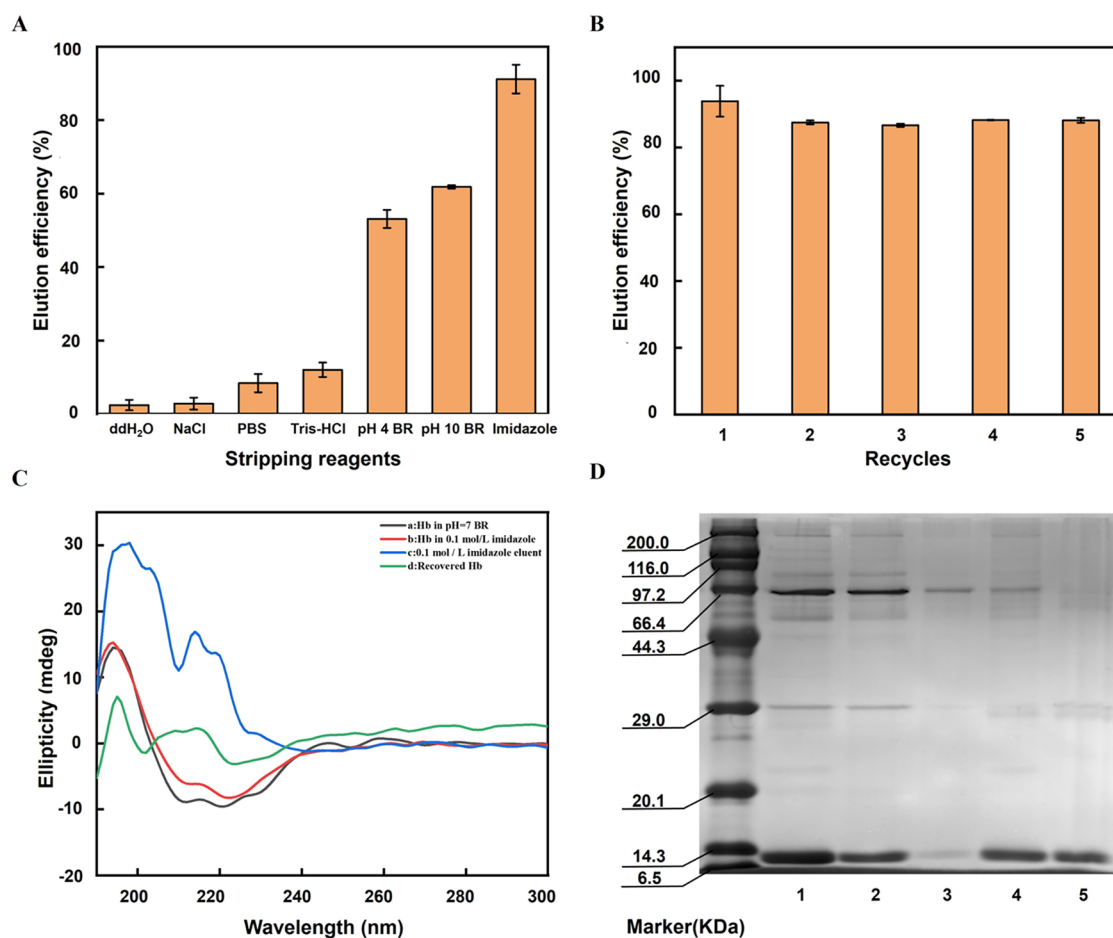


**Figure 3.** Evaluating Hb recovery and purification using the CMTO@Fe<sub>3</sub>O<sub>4</sub>-NH<sub>2</sub> composite: Recoveries of adsorbed Hb using various buffer solutions as elution reagents (A); the recyclability of Hb adsorption and elution (B); Soret region CD spectra of the structural integrity of Hb under varying conditions (C); SDS-PAGE results (D).

Based on these results and considering the influence of salt concentration typically found in real samples, the BR solution at pH 7.0 was selected as the protein solvent for further experiments.

The adsorption of Hb at different concentrations (100–900  $\mu\text{g mL}^{-1}$ ) was examined to explore the adsorption capacity of CMTO@Fe<sub>3</sub>O<sub>4</sub>-NH<sub>2</sub> for Hb. As shown in Figure 2D, the adsorption amount of Hb per unit of CMTO@Fe<sub>3</sub>O<sub>4</sub>-NH<sub>2</sub> increased with rising Hb concentration, indicating that the adsorption capacity of the material was directly proportional to the Hb concentration. However, the amount of Hb adsorbed per unit of CMTO@Fe<sub>3</sub>O<sub>4</sub>-NH<sub>2</sub> stabilized when the Hb concentration exceeded 800  $\mu\text{g mL}^{-1}$ , indicating that the adsorption capacity had approached saturation. This trend suggested that the adsorption of Hb onto CMTO@Fe<sub>3</sub>O<sub>4</sub>-NH<sub>2</sub> followed a monolayer adsorption mechanism. Additionally, the experimental data was consistent with the Langmuir adsorption model. As shown in Figure S1, a linear relationship was observed between  $1/q_{\text{eq}}$  and  $1/C_{\text{e}}$  with the corresponding linear relationship  $1/q_{\text{eq}} = 0.5809C_{\text{e}} + 0.0029$ , and a high correlation coefficient ( $R^2$ ) of 0.9931. The theoretical maximum adsorption capacity ( $Q_{\text{m}}$ ) was calculated to be 344.8  $\text{mg g}^{-1}$  based on this relationship.

#### Adsorption Mechanism of Hb on CMTO@Fe<sub>3</sub>O<sub>4</sub>-NH<sub>2</sub>

The adsorption of Hb onto CMTO@Fe<sub>3</sub>O<sub>4</sub>-NH<sub>2</sub> was mainly driven by the interaction between the enol structure<sup>31</sup> and triazole ring of CMTO and the  $\beta$ -subunits of Hb at pH 7.0 Hb

has no net charge at its isoelectric point (pI), which favors aggregation and reduces solubility. This aggregation exposed more hydrophobic amino acid residues on the Hb surface, thereby enhancing its interaction with the CMTO@Fe<sub>3</sub>O<sub>4</sub>-NH<sub>2</sub> composite and increasing adsorption efficiency.

As shown in Scheme 2, the molecular docking studies identified six key amino acid residues of Hb that interacted with CMTO. Specifically, Val- $\beta$ 137, Leu- $\beta$ 141, and Leu- $\beta$ 106 interact with the center of the triazole ring. Additionally, Val- $\beta$ 98 and Leu- $\beta$ 31 interact with the polyethyleneimine (PEI) component, while Phe- $\beta$ 103 interacts through the enol form of the triazole carbonyl group. The triazolinone ring exhibits conjugacy and hydrophobicity, which facilitates the interaction with the hydrophobic regions of Hb. Composed of nonpolar amino acid residues, these hydrophobic residues are localized through van der Waals interactions, promoting the binding of Hb to CMTO@Fe<sub>3</sub>O<sub>4</sub>-NH<sub>2</sub>. The nitrogen atoms in the triazolinone ring are electronegative, while the carbon atoms in the ring carry a positive charge. Meanwhile, Hb's amino acid side chains contain various charged groups, including the positively charged amino group of lysine, and the negatively charged carboxylic acid groups of aspartic acid and glutamic acid. The positive and negative charge regions of the CMTO@Fe<sub>3</sub>O<sub>4</sub>-NH<sub>2</sub> composite are attracted to the opposite charge groups of hemoglobin via electrostatic attraction, strongly stabilizing the binding of the two components. Various factors combine to determine the final binding situation.

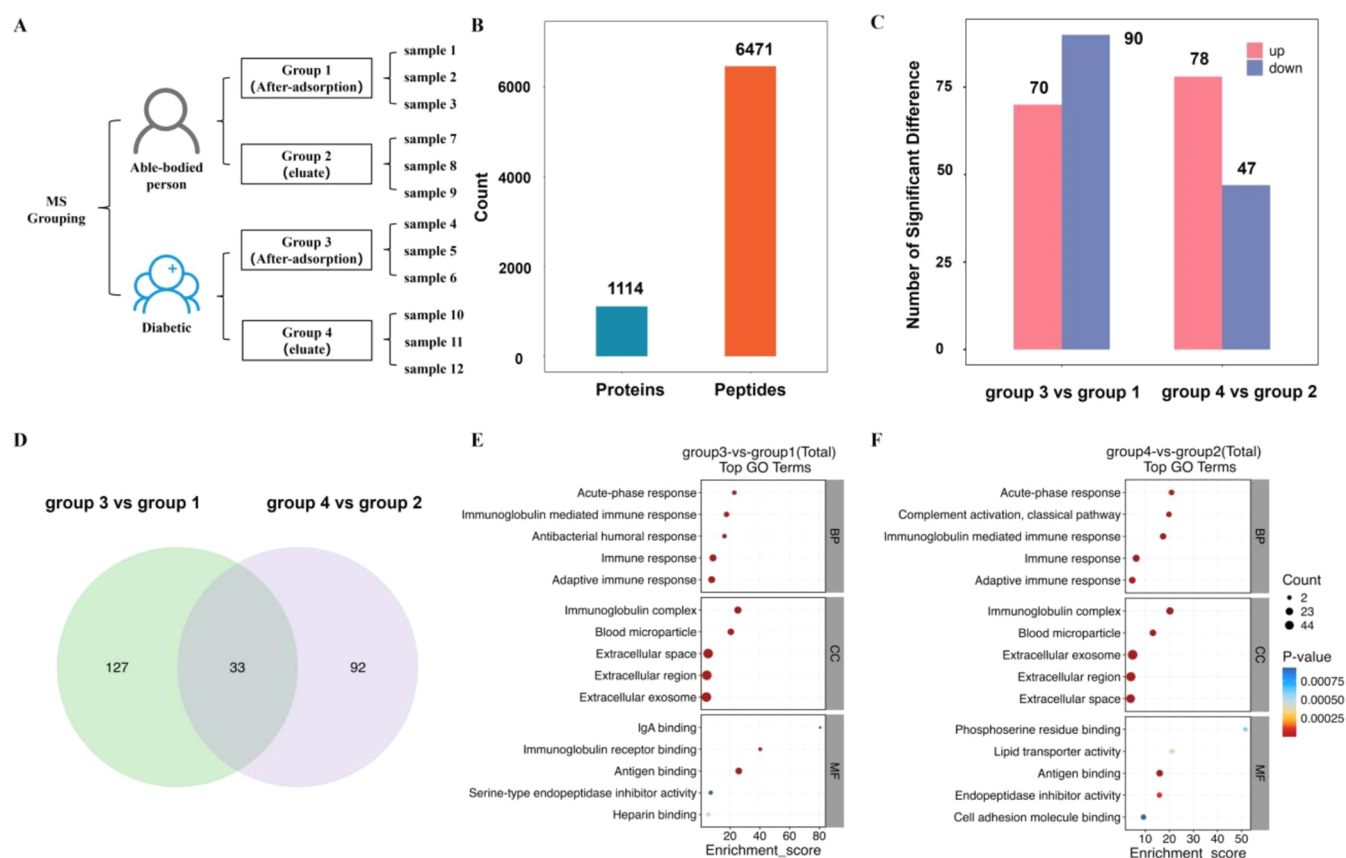


**Figure 4.** Experimental design diagram illustrating sample grouping (A); detection results of identified proteins and peptides (B); differentially expressed proteins (DEPs) (C); Venn Diagram of DEPs (D); GO functional enrichment analysis (Group 3 vs Group 1) (E); GO functional enrichment analysis (Group 4 vs Group 2) (F).

These specific interactions are crucial for the selective recognition and binding of Hb to CMTO@Fe<sub>3</sub>O<sub>4</sub>-NH<sub>2</sub>. Moreover, the binding energy between Hb and the ligand is low, suggesting a strong and stable binding affinity between CMTO and Hb. This robust interaction leads to the effective and reliable adsorption of Hb, making CMTO@Fe<sub>3</sub>O<sub>4</sub>-NH<sub>2</sub> an excellent adsorbent for hemoglobin recovery, particularly in biological applications.

**Elution and Reuse of Hb on CMTO@Fe<sub>3</sub>O<sub>4</sub>-NH<sub>2</sub>.** Various eluents were used in this study to effectively recover Hb adsorbed on CMTO@Fe<sub>3</sub>O<sub>4</sub>-NH<sub>2</sub> for further biological applications. The tested eluents included double-distilled water (ddH<sub>2</sub>O), 0.3 mol L<sup>-1</sup> NaCl, 0.05 mol L<sup>-1</sup> PBS, pH 6.8 Tris-HCl, pH 4.0 BR buffer, pH 10.0 BR buffer, 0.5% SDS, and 100 mmol L<sup>-1</sup> imidazole solution. As shown in Figure 3A, 100 mmol L<sup>-1</sup> imidazole solution exhibited the highest elution efficiency, achieving 91.2% Hb recovery. The adsorption and elution processes were repeated 5 times (Figure 3B), and the adsorption efficiency decreased slightly, which may be due to the slight shedding of CMTO functional groups or the aggregation of nanoparticles. In addition, multiple elution may cause surface structural wear and affect the adsorption performance.<sup>32</sup> However, the adsorption efficiency of the material in the whole process remains above 80.0%. This result demonstrates the excellent reusability of CMTO@Fe<sub>3</sub>O<sub>4</sub>-NH<sub>2</sub> in hemoglobin purification, highlighting its potential in applications that require multiple reuse cycles. Additionally, in order to investigate whether the hemoglobin recovered from the surface of CMTO@Fe<sub>3</sub>O<sub>4</sub>-NH<sub>2</sub> with 100 mmol L<sup>-1</sup>

imidazole solution as eluent was denatured, the conformational changes of hemoglobin were evaluated by circular dichroism spectroscopy (Figure 3C). In pH 7.0 BR buffer and 100 mmol L<sup>-1</sup> imidazole solution, the CD spectrum of Hb showed double negative peaks at 210 and 222 nm. After elution with 100 mmol L<sup>-1</sup> imidazole, the two peaks of Hb were 210 and 218 nm, respectively. Deviation to the right from the typical 206 and 220 nm double negative peak—peak values of hemoglobin  $\alpha$ -helix. In order to determine the cause of peak displacement, CD spectra of Hb solution after ultrafiltration after CMTO@Fe<sub>3</sub>O<sub>4</sub>-NH<sub>2</sub> adsorption and elution with 100 mmol L<sup>-1</sup> imidazole solution were recorded. The peaks obtained by this spectrum are 206 and 220 nm, which are highly coincident with the typical hemoglobin  $\alpha$ -helical conformation, indicating that the shift of the peaks to the right is reversible. This change may be due to excessive protein concentration and enhanced intermolecular interaction, resulting in protein aggregation,<sup>33</sup> thus affecting the characteristic peak position of CD spectrum. Furthermore, the increase of scattered light in a high concentration solution may also cause interference with the CD signal.<sup>34</sup> The results showed that CMTO@Fe<sub>3</sub>O<sub>4</sub>-NH<sub>2</sub> showed excellent biocompatibility, and the secondary structure of Hb was not irreversibly damaged during the adsorption and elution process. Therefore, the results show that CMTO@Fe<sub>3</sub>O<sub>4</sub>-NH<sub>2</sub> is a reliable adsorbent to ensure that the captured hemoglobin is suitable for subsequent applications and studies.

**Isolation and Purification of Hemoglobin from Human Whole Blood Samples.** Figure 3D shows the SDS-PAGE gel electrophoresis results of purified hemoglobin

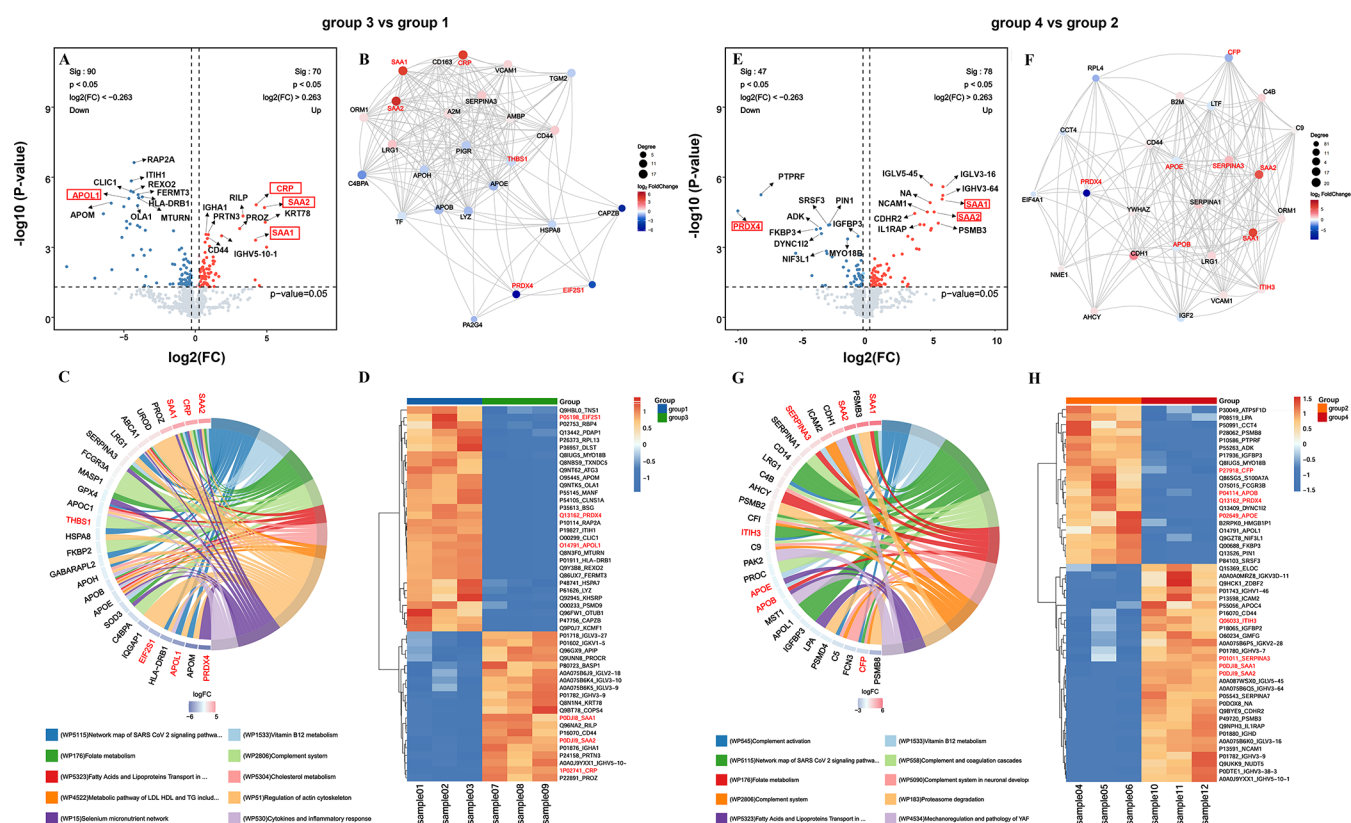


**Figure 5.** Proteomics profiling of group 3 vs group 1 and group 4 vs group 2: Volcano plot of differentially expressed proteins (A, E); protein–protein interaction (PPI) network analysis (B, F); WikiPathways enrichment analysis (Chord Diagram) (C, G); Heatmap of differentially expressed proteins (D, H).

(Hb) from human blood. In lane 1, containing protein extract from whole human blood, multiple protein bands were observed within the molecular weight range of 10–200 kDa, with a prominent band corresponding to Hb at approximately 10.0 kDa.<sup>35</sup> Meanwhile, the proteins adsorbed by CMTO@Fe<sub>3</sub>O<sub>4</sub>-NH<sub>2</sub> are shown in Lane 2. The intensity of the 10.0 kDa hemoglobin band was significantly reduced in this lane, indicating effective adsorption. Lane 3 shows the protein sample after a secondary water washing step, which helps remove some nonspecifically adsorbed proteins. Lane 4 displays the supernatant obtained after elution with a 100 mmol L<sup>-1</sup> imidazole solution, where the Hb band at 10.0 kDa is observed, consistent with the band detected prior to adsorption. In addition to this Hb band, minor extraneous bands were present in lane 4, likely resulting from the nonspecific adsorption of other proteins on the material or the enrichment of proteins that interact with hemoglobin. Furthermore, isolating Hb using CMTO@Fe<sub>3</sub>O<sub>4</sub>-NH<sub>2</sub>, enables the enrichment and characterization of Hb-binding proteins, offering valuable insights into the protein–protein interactions and the biological pathways associated with hemoglobin.

#### Biomarker Discovery in Diabetic Blood Proteomics.

As illustrated in Figure 4A, a comparison between Group 1 and Group 3 exhibited differences in the supernatants of diabetic patients and healthy individuals after CMTO@Fe<sub>3</sub>O<sub>4</sub>-NH<sub>2</sub> adsorption. This comparison helped analyze the differences in many low-abundance proteins in the supernatant after removing high-abundance Hb. The comparison between Group 2 (eluent from normal samples) and Group 4 (eluent from normal samples) identified the high-abundance proteins

captured and subsequently eluted by CMTO@Fe<sub>3</sub>O<sub>4</sub>-NH<sub>2</sub>, providing insights into variations between healthy individuals and those with diabetes. This comparison can reveal variations in abundant proteins typically found in blood, such as Hb and other major plasma proteins, that may be linked with the pathological state of diabetes. Identifying these differences can provide valuable insights into the underlying molecular mechanisms of diabetes and potentially uncover high-abundance protein biomarkers associated with the disease.

After adsorption and elution with CMTO@Fe<sub>3</sub>O<sub>4</sub>-NH<sub>2</sub>, whole blood samples from diabetic patients and normal subjects were analyzed using a proteomic technique called Data Independent Acquisition (DIA). As shown in Figure 4B, the results of protein sequencing revealed 1114 proteins and 6471 peptides. As shown in Figure 4C, 70 proteins were significantly upregulated while 90 proteins were significantly downregulated in Group 1 compared to Group 3 (determined by  $p < 0.05$  and  $FC \geq 1.2$  or  $FC \leq 1/1.2$ ; See Supporting Table S1). Similarly, compared to Group 4, 78 proteins were upregulated while 47 proteins were significantly downregulated in Group 2 (determined by  $p < 0.05$  and  $FC \geq 1.2$  or  $FC \leq 1/1.2$ ; see Supporting Table S2). As shown in Figure 4D, a total of 252 differential proteins (ratio  $\leq \pm 1.3$ ,  $p < 0.05$ ) were identified. Furthermore, Gene Ontology (GO) analysis revealed significant enrichment in molecular function, cellular component, and biological process categories. Notably, the top three enriched biological processes were associated with immune response and acute-phase response. In terms of cellular components, differential proteins were predominantly localized to the extracellular environment, especially within exosomes and immune complexes. Meanwhile, the molecular



function analysis revealed that most proteins, including binding of IgA and immunoglobulins, were enriched in immune-related functions, (Figure 4E,4F).

In Figure 5, the volcano plot illustrates the distribution of all differentially expressed proteins between Group 1 and Group 3 (Figure 5A). As shown in Figure 5B, the differential protein interaction network analysis revealed that upregulated proteins, such as *CRP*, *SAA1*, and *SAA2*, are primarily involved in acute-phase response and inflammatory response. Thus, these proteins may serve as potential markers of inflammation in diabetic patients. Conversely, downregulated proteins, such as *PRDX4*, and *EIF2S1* may be associated with antioxidant stress and protein synthesis regulation, reflecting metabolic imbalance in patients with diabetes. Additionally, after statistical analysis and screening, highly connected proteins like *THBS1* likely act as key regulatory nodes in these pathways. A comparison between the healthy and control groups revealed that the supernatant from the composite material-treated surfaces showed significantly upregulated proteins such as *SAA1*, *SAA2*, and C-reactive protein (*CRP*). Meanwhile, the most significantly downregulated proteins included thiol-specific peroxidase (*PRDX4*) and eukaryotic translation initiation factor 2 subunit  $\alpha$  (*EIF2S1*). Thrombospondin1- (*THBS1*), Apolipoprotein C-1 (*APOL1*). WikiPathways enrichment analysis (Figure 5C) revealed that these proteins were primarily enriched in immune-related, metabolism-related, and inflammatory response pathways. Notably, genes such as *APOL1*, *THBS1*, *C4A*, and *C4BPA* are involved in multiple pathways and may play crucial roles in immune metabolism processes. As shown in Figure 5D, the top 50 differential proteins were selected for clustering analysis.

In Figure 5 the volcano plot illustrates the distribution of differential proteins between Group 2 and Group 4 (Figure 5E). As shown in Figure 5F, the differential protein interaction network analysis revealed the significant upregulation of *SAA1* and *SAA2*, underscoring the importance of inflammatory activation in diabetic patients. Conversely, the downregulation of *PRDX4* and *CFP* suggests a potential reduction in oxidative stress during diabetes progression. Metabolism-related proteins, such as *SERPINA3*, *APOE*, and *APOB* are potential key regulatory targets. After statistical analysis and screening, significantly upregulated proteins in diabetic patients compared with the healthy control group included *SAA1*, *SAA2*, plasma protein *SERPINA3*, and  $\alpha$ -1 interalpha-trypsin inhibitor heavy chain 1 (*ITIH3*). Conversely, the most significantly downregulated proteins included apolipoproteins, such as *APOE*, *APOB*, and *CFP*. As shown in Figure 5G, the WikiPathways enrichment analysis indicated that differential proteins were predominantly associated with the complement system, inflammation, metabolism, and degradation, as well as the immune and virus response pathways. Genes such as *SAA1*, *SAA2*, and *APOE* are involved in multiple pathways, emphasizing their crucial roles in complement system and metabolic regulation. The top 50 differential proteins were selected for clustering analysis (Figure 5H). Therefore,  $\text{CMTO@Fe}_3\text{O}_4\text{-NH}_2$  was used to extract Hb, establishing a novel method for whole blood processing. The findings of this study identified the following 12 potential disease biomarkers in the diabetic group: *SAA1*, *SAA2*, *CRP*, *SERPINA3*, *ITIH3*, *PRDX4*, *EIF2S1*, *THBS1*, *APOL1*, *APOE*, *APOB*, and *CFP*.

## CONCLUSIONS

This study reports the successful synthesis of magnetic nanoparticles modified with 3-chloromethyl-1,2,4-triazolin-5-one ( $\text{CMTO@Fe}_3\text{O}_4\text{-NH}_2$ ) and characterized them using FT-IR, Raman spectroscopy, SEM, TEM, EDS, and magnetic performance testing curves. At pH 7.0, the unique enolic form of CMTO along with the specific interaction of the triazole ring with the  $\beta$ -subunit of hemoglobin, endowed the  $\text{CMTO@Fe}_3\text{O}_4\text{-NH}_2$  composite with excellent biocompatibility and remarkable hemoglobin-binding efficiency. As a result, the prepared composite material was employed for the solid-phase extraction of Hb from human whole blood, offering a reliable and efficient method for separating and purifying Hb. Notably, the development of this approach provides a strong foundation for advancing proteomics research. Through the application of this technique 12 potential diabetes-related biomarkers were identified, providing fresh insights into the underlying mechanisms of the disease. These findings not only deepen our understanding of Hb-related disorders but also underscore the potential of drug-modified magnetic nanoparticles for selective binding, separating, and purifying target proteins. This approach holds significant promise for advancing both diagnostic and therapeutic strategies in the fight against diabetes and other related diseases.

## ASSOCIATED CONTENT

### Supporting Information

The Supporting Information is available free of charge at <https://pubs.acs.org/doi/10.1021/acs.analchem.5c00759>.

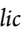
Chemicals and apparatus; preparation of  $\text{Fe}_3\text{O}_4\text{-NH}_2$ ; protein adsorption/desorption by  $\text{CMTO@Fe}_3\text{O}_4\text{-NH}_2$ ; the samples were divided into the following four groups; adsorption capacity Plot of  $1/q_{\text{eq}}$  against  $1/C_{\text{eq}}$  (Figure S1); optimization of adsorption temperature and time; effect of temperature on adsorption efficiency (A); effect of time on adsorption efficiency (B) (Figure S2); after detect and analyze by mass spectrometry (Table S1); after detect and analyze by mass spectrometry (Table S2) (PDF)

## AUTHOR INFORMATION

### Corresponding Authors

**Mingsheng Zhou** – Shenyang Key Laboratory of Vascular Biology, Science and Experiment Center, Shenyang Medical College, Shenyang 110034, People's Republic of China; Email: [zhoums1963@163.com](mailto:zhoums1963@163.com)

**Fu Ren** – Shenyang Key Laboratory for Phenomics, Liaoning Province Key Laboratory for Phenomics of Human Ethnic Specificity and Critical Illness, Shenyang Medical College, Shenyang 110034, People's Republic of China; Email: [rf@symc.edu.cn](mailto:rf@symc.edu.cn)

**Qing Chen** – School of Pharmacy, Shenyang Medical College, Shenyang 110034, People's Republic of China;  [orcid.org/0000-0001-6251-8292](https://orcid.org/0000-0001-6251-8292); Email: [chenqing0906@symc.edu.cn](mailto:chenqing0906@symc.edu.cn)

### Authors

**Xinze Wu** – School of Pharmacy, Shenyang Medical College, Shenyang 110034, People's Republic of China

**Lingxi Zhang** – School of Pharmacy, Shenyang Medical College, Shenyang 110034, People's Republic of China

**Tian Luan** — School of Pharmacy, Shenyang Medical College, Shenyang 110034, People's Republic of China; [orcid.org/0000-0003-4284-7990](https://orcid.org/0000-0003-4284-7990)

**Ying Wang** — School of Pharmacy, Shenyang Medical College, Shenyang 110034, People's Republic of China

**Xiangyu Liu** — School of Pharmacy, Shenyang Medical College, Shenyang 110034, People's Republic of China

**Xifan Mei** — Liaoning Vocational College of Medicine, Shenyang 110101, People's Republic of China; [orcid.org/0000-0003-3698-0525](https://orcid.org/0000-0003-3698-0525)

**Xuwei Chen** — Research Center for Analytical Sciences, Department of Chemistry, College of Sciences, Northeastern University, Shenyang 110819, People's Republic of China; [orcid.org/0000-0001-7189-5022](https://orcid.org/0000-0001-7189-5022)

**Jianhua Wang** — Research Center for Analytical Sciences, Department of Chemistry, College of Sciences, Northeastern University, Shenyang 110819, People's Republic of China; [orcid.org/0000-0003-2175-3610](https://orcid.org/0000-0003-2175-3610)

Complete contact information is available at:

<https://pubs.acs.org/10.1021/acs.analchem.5c00759>

## Author Contributions

<sup>#</sup>X.W. and L.Z. contributed equally to this work.

## Notes

**Ethical Approval** This study was reviewed and approved by Ethics Committee of Shenyang Medical College (2024 Ethics Review No. 4).

The authors declare no competing financial interest.

## ACKNOWLEDGMENTS

The authors appreciate the financial support from the National Natural Science Foundation of China (21804093), Liaoning Province Science and Technology General Project by Central Government (2023-MS-324), Liaoning Province Department of Education Self-selected Project (LJ212410164028) and Shenyang Young and Middle-aged Science and Technology Innovation Talent Project (RC230168).

## REFERENCES

- (1) Nowak-Jary, J.; Machnicka, B. *Int. J. Nanomed.* **2023**, *18*, 4067–4100.
- (2) Ul-Islam, M.; Ullah, M. W.; Khan, S.; Manan, S.; Khattak, W. A.; Ahmad, W.; Shah, N.; Park, J. K. *Environ. Sci. Pollut. Res.* **2017**, *24*, 12713–12722.
- (3) Araújo, E.; Carneiro, S. V.; Neto, D. M. A.; Freire, T. M.; Costa, V. M.; Freire, R. M.; Fechine, L. M. U. D.; Clemente, C. S.; Denardin, J. C.; dos Santos, J. C. S.; Santos-Oliveira, R.; Rocha, J. S.; Fechine, P. B. A. *Adv. Colloid Interface Sci.* **2024**, *328*, No. 103166.
- (4) Chu, Z.; Song, Y.; Wu, M.; Zhu, M.; Meng, B.; Zhao, Y.; Zhai, R.; Dai, X.; Fang, X. *Anal. Chem.* **2024**, *96*, 14099–14107.
- (5) Lin, H.; Ou, J.; Liu, Z.; Wang, H.; Dong, J.; Zou, H. *Anal. Chem.* **2015**, *87*, 3476–3483.
- (6) Han, H.; Sohn, B.; Choi, J.; Jeon, S. *Open Biomed. Eng. Lett.* **2021**, *11*, 297–307.
- (7) Chen, G.; Roy, I.; Yang, C.; Prasad, P. N. *Chem. Rev.* **2016**, *116*, 2826–2885.
- (8) Jain, R. K.; Stylianopoulos, T. *Nat. Rev. Clin. Oncol.* **2010**, *7*, 653–664.
- (9) Petrilli, R.; Pinheiro, D. P.; de Cássia Evangelista de Oliveira, F.; Galvão, G. F.; Marques, L. G. A.; Lopez, R. F. V.; Pessoa, C.; Eloy, J. O. *Curr. Med. Chem.* **2021**, *28*, 2485–2520.
- (10) Cullis, P. R.; Felgner, P. L. *Nat. Rev. Drug Discovery* **2024**, *23*, 709–722.
- (11) Lin, G.; Zhang, M. *Acc. Chem. Res.* **2023**, *56*, 1578–1590.
- (12) Busatto, S.; Pham, A.; Suh, A.; Shapiro, S.; Wolfram, J. *Biomed. Microdevices* **2019**, *21*, No. 46.
- (13) Zhang, C.; Yan, L.; Wang, X.; Zhu, S.; Chen, C.; Gu, Z.; Zhao, Y. *Nano Today* **2020**, *35*, No. 101008.
- (14) Alizadeh, L.; Zarebkohan, A.; Salehi, R.; Ajjoolabady, A.; Rahmati-Yamchi, M. *J. Drug Targeting* **2019**, *27*, 839–852.
- (15) Aryutova, K.; Stoyanov, D. S.; Kandilarova, S.; Todeva-Radneva, A.; Kostianev, S. S. *Curr. Pharm. Des.* **2021**, *27*, 4039–4048.
- (16) Li, W.; Shao, C.; Zhou, H.; Du, H.; Chen, H.; Wan, H.; He, Y. *Ageing Res. Rev.* **2022**, *81*, No. 101730.
- (17) Ahmad, A.; Imran, M.; Ahsan, H. *Pharmaceutics* **2023**, *15*, No. 1630.
- (18) Geyer, P. E.; Holdt, L. M.; Teupser, D.; Mann, M. *Mol. Syst. Biol.* **2017**, *13*, No. 942.
- (19) Dayon, L.; Cominetti, O.; Affolter, M. *Expert Rev. Proteomics* **2022**, *19*, 131–151.
- (20) Anderson, N. L.; Anderson, N. G. *Mol. Cell. Proteomics* **2002**, *1*, 845–867.
- (21) Li, F.; Lu, L.; Gao, D.; Wang, M.; Wang, D.; Xia, Z. *Talanta* **2018**, *185*, 528–536.
- (22) Zhao, Q.; Fang, F.; Wu, C.; Wu, Q.; Liang, Y.; Liang, Z.; Zhang, L.; Zhang, Y. *Anal. Chim. Acta* **2016**, *912*, 58–64.
- (23) Trinh, D. N.; Gardner, R. A.; Franciosi, A. N.; McCarthy, C.; Keane, M. P.; Soliman, M. G.; O'Donnell, J. S.; Meleady, P.; Spencer, D. I. R.; Monopoli, M. P. *ACS Nano* **2022**, *16*, 5463–5475.
- (24) Chen, M. L.; Chen, M. L.; Chen, X. W.; Wang, J. H. *Macromol. Biosci.* **2010**, *10*, 906–915.
- (25) Hallez, F.; Combès, A.; Desoubries, C.; Bossée, A.; Pichon, V. *J. Chromatogr. A* **2022**, *1665*, No. 462830.
- (26) Ma, W.; Xu, S.; Li, J.; Guo, J.; Lin, Y.; Wang, C. *J. Polym. Sci., Part A: Polym. Chem.* **2011**, *49*, 2725–2733.
- (27) Dutta, S. S.; Lourderaj, U. *J. Phys. Chem. A* **2025**, *129*, 1293–1300.
- (28) Feng, H.; Li, R.; Wu, Y.; Liu, X. *ChemPhysChem* **2024**, *25*, No. e202300525.
- (29) Giricz, A.; Czako, G.; Papp, D. *Chemistry* **2023**, *29*, No. e202302113.
- (30) Zhang, F.; Cao, H.; Yue, D.; Zhou, Z. *J. Phys. Chem. C* **2013**, *117*, 3513–3519.
- (31) Eryilmaz, S.; Bagdatli, E. *J. Mol. Graphics Modell.* **2024**, *131*, No. 108814.
- (32) Binandeh, M.; Karimi, F.; Rostamnia, S. *Int. J. Health Sci.* **2021**, *15*, 3–8.
- (33) Kurinomaru, T.; Shiraki, K. *Int. J. Biol. Macromol.* **2017**, *100*, 11–17.
- (34) Gregory, R. P. F.; Raps, S. *Biochem. J.* **1974**, *142*, 193–201.
- (35) Yang, M.; Dong, Q.; Guan, Y.; Zhang, Y. *Biomacromolecules* **2023**, *24*, 1233–1243.